INSTITUTE OF PHYSICS PUBLISHING PHYSICS IN MEDICINE AND BIOLOGY

Phys. Med. Biol. **48** (2003) 543–559 PII: S0031-9155(03)52284-9

Models and measurements of light intensity changes during laser interstitial thermal therapy: implications for optical monitoring of the coagulation boundary location

Lee C L Chin[1,2], William M Whelan[2,3] and I Alex Vitkin[1,2,4]

[1] Medical Physics Division, Ontario Cancer Institute/Princess Margaret Hospital, University Health Network, University of Toronto, 610 University Avenue, Toronto, Ontario, Canada M5G 2M9
[2] Department of Medical Biophysics, University of Toronto, 610 University Avenue, Toronto, Ontario, Canada M5G 2M9
[3] Department of Mathematics, Physics and Computer Science, Ryerson University, 350 Victoria Street, Toronto, Ontario, Canada M5B 2K3
[4] Department of Radiation Oncology, University of Toronto, 610 University Avenue, Toronto, Ontario, Canada M5G 2M9

Received 13 August 2002
Published 5 February 2003
Online at stacks.iop.org/PMB/48/543

Abstract

We have developed a multi-region spherical Monte Carlo (MC) model to simulate the dynamic changes in light intensity measured during laser interstitial thermal therapy (LITT). Model predictions were validated experimentally in tissue-simulating albumen phantoms with well-characterized optical properties that vary dynamically with LITT in a way similar to tissue.

For long treatments (2.5 W, ∼1800 s), the transient light intensity changes demonstrated better qualitative agreement with a three-region MC model (with an inner layer of fully coagulated optical properties, a middle layer of partially coagulated properties and an outer region of native properties); for short treatments (4 W, ∼240 s), better qualitative agreement was seen with a two-region MC model (with an inner layer of fully coagulated properties and outer region of native properties). These differences were attributed to differences in coagulation formation during low- and high-powered heating regimes, respectively. At the end of heating, a three-region coagulation zone was observed for both heating schemes. Quantitatively, final light intensity changes at the end of heating were compared with changes predicted by both two- and three-region MC for the same experimentally measured coagulation size and found to agree within ∼30% for both models. The developed MC model helps lend insight into the nature of thermal coagulation events occurring for low and high power LITT irradiation schemes.

1. Introduction

Laser interstitial thermal therapy (LITT) is a developing, minimally invasive technique for the treatment of solid tumours (Roggan and Muller 1995). During LITT, laser energy is delivered interstitially using thin optical fibres to induce coagulative necrosis of the target site by elevating the tissue temperatures to 55–90 °C. The goal of the treatment is to completely coagulate the target site while sparing healthy surrounding tissue. Real-time monitoring of the treatment is important, as *a priori* determination of final coagulation size using treatment planning models is difficult due to dynamic changes in optical, thermal and blood flow properties induced by thermal coagulation.

Online monitoring of tissue coagulation can be performed directly or indirectly. Indirect methods measure the temperature elevation of the target site and apply time–temperature relationships for cell death to infer the extent of tissue damage. Magnetic resonance imaging (MRI) thermometry has been successfully applied for this technique (Vitkin *et al* 1997, Eyrich *et al* 2000, Sherar *et al* 2000) while strategically placed point temperature sensors, though offering a sparser map of tissue temperature, have proven an economical and practical alternative (Sherar *et al* 2001, Wohlgemuth *et al* 2001). The primary weakness of indirect methods is that calculation of coagulation is highly dependent on the specific thermal damage parameters of the tissue being treated, which are generally unknown. More direct means of damage monitoring involve the measurement of tissue properties sensitive to coagulation induced structural changes. Ultrasound (Bevan and Sherar 2001, Bennedbaek *et al* 2001), MRI (Sherar *et al* 2000, Bremer *et al* 2002) and computed tomography (Purdie *et al* 2000), have all been explored as possible imaging modalities for direct mapping of thermal damage.

As an alternative to the above methods, we have recently demonstrated the potential of optical measurements, which track changes in interstitial light intensity using strategically placed optical sensors for the direct monitoring of LITT (Chin *et al* 2001, Whelan *et al* 2001). This method takes advantage of the significant changes in tissue optical scattering that occurs due to thermal coagulation (Skinner *et al* 2000, Ritz *et al* 2001). Therefore, during LITT, a growing coagulation front will result in a dynamically changing light distribution directly related to the extent of thermal damage.

For the purposes of LITT treatment planning, previous investigators have attempted to model dynamic changes in light distribution by incorporating multi-region Monte Carlo (MC) (Roggan and Muller 1995), finite element (Whelan 1996) and diffusion theories (Iizuka *et al* 2000) light models into opto-thermal simulations of thermal lesion formation. Validation of these models has generally focussed on final lesion size or temperature rise generated in phantoms or *ex vivo* tissue and not on changes in interstitial light intensity. Few investigations have examined the possibility of employing interstitial changes in light intensity to assess thermal damage during LITT. Svaasand *et al* (1999) and Pham *et al* (2000) have explored the use of frequency-domain reflectance measurements to evaluate deep burns near the skin surface. However, to our knowledge, there have been no attempts to utilize light models and interstitial measurements as a means of assessing coagulation size during LITT.

The goal of this paper is to examine the ability of a multi-region spherical light model (with regions of I: fully coagulated, II: partially coagulated and III: native optical properties) to relate dynamic changes in light intensity measured interstitially during LITT to the location of the coagulation boundary. Though diffusion theory has previously been applied in parameter estimation procedures to determine the optical properties of multi-layered tissue (Alexandrakis *et al* 1998, Kienle *et al* 1998), the model is inaccurate close to sources, near boundaries and in highly absorbing materials (Patterson *et al* 1991, Martelli *et al* 2000). However, it is expected that optical monitoring, in certain clinical situations may necessitate the placement of sensors within 2–3 mm of a source and in highly absorbing tissues (such as liver). Therefore, to ensure that differences between experimental and theoretical results are not due to the proximity of the sensor location to the source fibre, we have developed multi-region MC models and validated our results experimentally in well-characterized albumen phantoms (Iizuka *et al* 1999). Since the boundary between coagulated and native tissue often exhibits a gradual gradient and not a sharp demarcation, we have compared two-region and three-region MC simulations. The three-region simulation attempts to represent a coagulation gradient with region I using completely coagulated properties, region II using partially coagulated properties and region III using native properties, while the two-region model assumes a distinct demarcation between regions I (fully coagulated) and II (native) (i.e., region of partial coagulation not present). The importance of this study is that it offers additional insight and understanding into the types of light models that should be applied for modelling transient light intensity in treatment planning simulations and in optical monitoring strategies for coagulation boundary determination.

2. Theory

Monte Carlo simulations are well described in the literature (Wilson and Adam 1983, Wang *et al* 1995) and only the salient features of our model will be reviewed here. MC simulations trace the propagation of individual photons through a turbid medium until the photon experiences complete absorption or escapes from the medium. Photon movement is determined by random number sampling (between 0 and 1) weighted according to the scattering (μ_s) and absorption (μ_a) coefficients of the medium being simulated. In a similar way, scattering angles are sampled randomly based on an appropriate scattering phase function. By tracking a sufficient number of photons, an accurate statistical representation of the internal light intensity can be generated.

Our program was modified from the shareware MC code by Wang *et al* (1995) for layered turbid media. In our simulations, an isotropic point source with a delta function pulse originating at $(x_c, y_c, z_c) = (0, 0, 0)$ was used. The Henyey–Greenstein phase function characterized by the anisotropy factor, g, was used to sample the azimuthal angle of scattering (Henyey and Greenstein 1941) while the polar angle was sampled evenly over 2π. Since the photon path is a directional vector, ray-tracing techniques can be used to determine its intersection with the boundary of a different optical media (e.g., a photon passing from a region of coagulated to a region of normal tissue). A ray-tracing algorithm for spherical media (described in detail in the appendix) was utilized with MC modelling to determine the light distribution from a spherical 2 mm diameter CW source surrounded by concentric spheres of different optical properties (figure 1). Instead of testing for intersection with an individual voxel (e.g., De Jode 1999), the ray-tracing algorithm allows a global definition for intersection with an irregularly shaped object by testing for photon intersection determined by the solutions of a quadratic equation, t_1 and t_2, and its discriminant, $\bar{D}$ (see the appendix). As shown in figure 1, a photon located in a spherical region I can either cross up to region I + 1 or down to region I − 1. In the algorithm, we first test for potential intersection with the inner sphere by calculating $\bar{D}$ for region I − 1. If $\bar{D} > 0$, and both t_1 and t_2 are positive, then the smallest t is chosen to be the photon distance to the sphere surface. If the MC sampled path length in the current layer, s, is greater than the chosen t, then the photon is propagated to the boundary and the remaining path length, s_2, is recalculated according to the optical properties, $\mu_t = \mu_s + \mu_a$, of region I − 1 using

$$s_2 = (s - t)\frac{\mu_{t_1}}{\mu_{t_2}}. \tag{1}$$

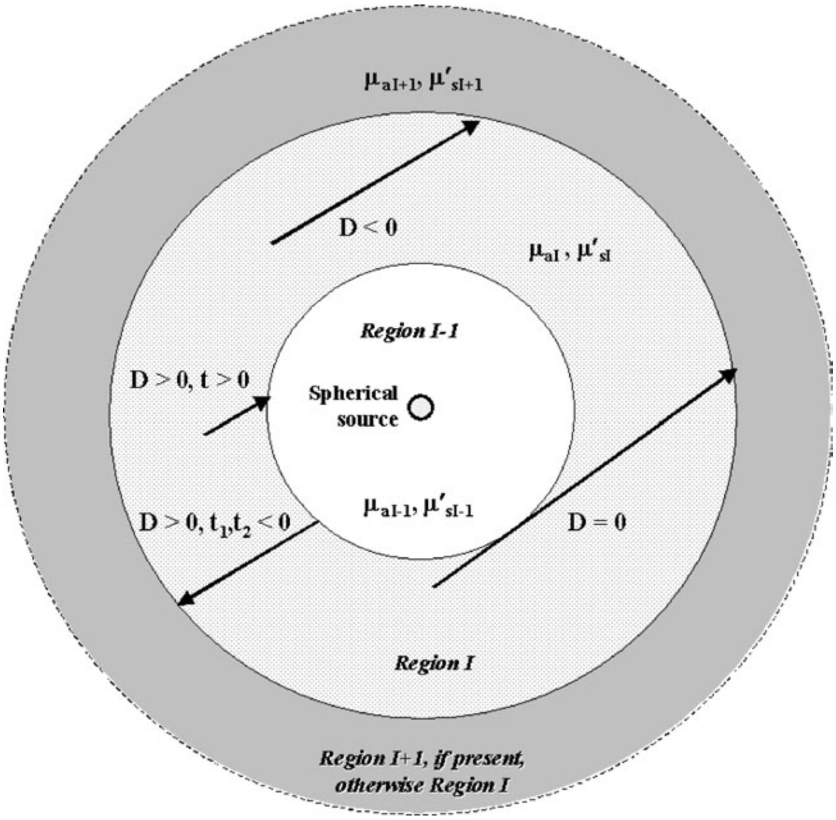

Figure 1. Spherical multi-layered structure. A ray located in region I can undergo four possible interactions with region I − 1: (a) $D > 0$, $t_{1,2} > 0$ hits, (b) $D > 0$, $t_{1,2} < 0$ misses, (c) $D = 0$ (any t) skims, (d) $D < 0$ (any t) misses. A ray-missing region I − 1 will hit region I + 1. Due to tissue scattering, the photon step size must be greater than the value of t for the ray to intersect. See the appendix for details.

If $\bar{D} \leqslant 0$ or both $t < 0$ for region I −1, the discriminant is then calculated for region I + 1 and a similar process is repeated. Note that if a photon is located in the innermost layer, $I = 1$ (e.g., the layer surrounding a point source or the diameter of the source fibre for a finite source), then the photon is only tested for transmission to the upper layer.

Multi-region spherical MC used native and coagulated optical properties of albumen phantoms from our previous studies at 805 nm (Iizuka *et al* 1999). The MC simulations were run using optical properties for completely native, completely coagulated and partially coagulated albumen phantoms with coagulation radii between 0 and 10 mm. The source fibre was modelled as a 2 mm diameter sphere with optical properties set at $\mu_a = 0$ cm^{-1} and $\mu_s' = (1 - g)\mu_s = 1$ cm^{-1}. The optical properties of albumen phantoms (Iizuka *et al* 1999) are shown in table 1. As the anisotropy factor, g, was not previously characterized, we assumed $g = 0.9$ (typical for biological tissues) and scaled the scattering coefficient according to the known reduced scattering coefficient using $\mu_s = \mu_s'/(1 - g)$. Two-region MC simulations were performed with region I using completely coagulated properties and region II using native properties (table 1). Three-region MC simulations were also run, with region I using completely coagulated properties, region II using partially coagulated properties and region III using native properties (table 1). Based on experimental observations, region II was

Table 1. Optical properties used in MC simulations.

Tissue	μ_a (cm^{-1})	μ_s (cm^{-1})	g	Wavelength (nm)	Reference
Albumen phantom (N)	0.5	26.7	0.9	805	Iizuka *et al* (1999)
Albumen phantom (PC)	0.6	65.5	0.9	805	Iizuka *et al* (1999)
Albumen phantom (C)	0.7	131	0.9	805	Iizuka *et al* (1999)
Bovine liver (N)	0.5	120	0.92	850	Roggan and Muller (1995)
Bovine liver (C)	1.7	480	0.91	850	Roggan and Muller (1995)
Human prostate (N)	0.6	100	0.94	850	Roggan and Muller (1995)
Human prostate (C)	0.7	230	0.94	850	Roggan and Muller (1995)

N = native, PC = partially coagulated, C = coagulated.

set as a constant radius of 1 mm surrounding region I that increased as region I increased in radius. Each MC was run using one million photons to achieve statistically meaningful results while minimizing variance.

3. Materials and methods

Albumen phantoms were solidified in an acrylic fluence box of dimensions 6 cm × 6 cm × x cm. A plastic jig was fixed above the fluence box allowing for the positioning of multiple detector fibres (1.2 mm diameter, Cardiofocus, Boston, MA) at set positions of 1.5–4 mm parallel to the spherical source fibre (2 mm diameter, Cardiofocus). A separate 800 μm detection fibre (Cardiofocus) was aligned perpendicular to the source fibre and attached to a micrometre translation stage (Thorlabs Inc., Newton, NJ), allowing for radial fluence scans at 0.5 mm steps throughout the 8 → 0 mm distance from the source. The 800 μm sensor was chosen solely on availability and had a similar response to the 1.2 mm detectors. The source fibre was connected to a Diomed-15 laser (Diomed Ltd, Cambridge, UK) with power output between 0.5 and 15 W at 805 nm. PDA55 photodiodes (Thorlabs Inc., Newton, NJ) were used to convert the collected light into photovoltage signals proportional to the light intensity or fluence (Van Staveren *et al* 1995).

Dynamic light intensity changes were measured during LITT of albumen phantoms. The albumen phantoms composed of naphthol green dye, albumen stock and agar are well characterized optically and provide a homogeneous medium (whose optical properties are dynamic in response to heating) for model validation of opto-thermal denaturations (Iizuka *et al* 1999). Detection fibres were pre-positioned in the fluence box with the liquid phantom mixture poured afterwards into the box to solidify around the fibres.

Albumen phantoms were irradiated using three heating schemes: (a) 2.5 W for 200 s, (b) 2.5 W for 1500–1800 s and (c) 4 W for 240–360 s. The heating schemes were chosen to determine if our models were valid for both high power and low power treatments.

During heating, changes in light intensity obtained from the photodiodes were recorded using a Gen 2000 multifunction data acquisition system (Labmate Sciemetrics, Nepean, Canada) displaying the average of 30 photovoltage signals at fixed positions (1.5–4 mm) from the source at an update rate of 1 Hz. Following heating, samples were allowed to cool and a spatial fluence scan was performed at a non-coagulating power of 0.5 W using the 800 μm dosimetry fibre by advancing it through the gel phantom towards the source (8 → 0 mm). Phantoms were then cut at the central plane and coagulation sizes measured visually using a ruler and photographed using a digital camera. Given the ruler resolution of 0.5 mm and

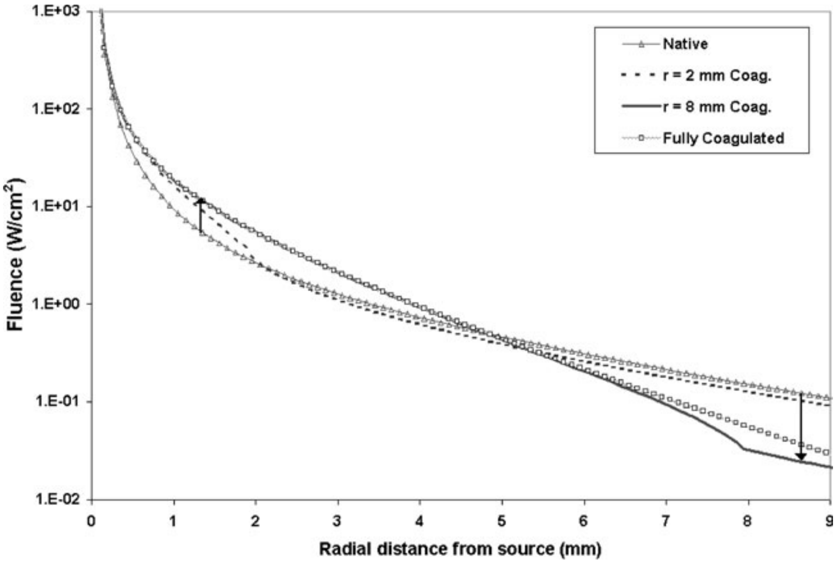

Figure 2. MC simulation of two-region spatial fluence distribution for albumen phantoms. Note that as the coagulation front passes the 2 mm position, an increase in fluence occurs inside 2 mm (up arrow), while as the coagulation front approaches the 8 mm position, a decrease in fluence results (down arrow). The power was nominally chosen to be 1 W.

some uncertainty in locating the central plane of coagulation, an estimated error of 0.5 mm was attributed to the visually measured coagulation radius.

4. Results

4.1. Two-region and three-region Monte Carlo simulations

Figure 2 shows the spatial fluence distribution, as predicted by a two-region MC for albumen phantoms with final coagulation radii of 2 and 8 mm, respectively. Fluence distributions for completely native and coagulated phantom have also been plotted. Results are on a log scale to help delineate the key features of the graph.

Examining the fully coagulated and native curves, it is clear that the increased scattering properties of coagulated phantom results in a steeper fluence fall-off than native properties. In the partially coagulated cases, within the region of coagulation, fluence falls off sharply, similar to the purely coagulated case, while outside the coagulation radius the fluence tends to fall off as that of the native case. There is also a sharp transition zone, marking the location of the coagulation boundary, where the fluence drops steeply before converging to the native slope.

Note that fluence at positions within 2 mm increases while fluence outside of 8 mm decreases relative to the native fluence, as the coagulation radius increases from 2 to 8 mm. Represented in another way, figure 3(a) shows the relative fluence at sensor positions between 1.5 and 9 mm due to increasing coagulation radii, r_{coag}. Relative values are defined as the ratio of the fluence readings for a given coagulation radius, $\Phi(r_{\mathrm{coag}})$, divided by the fluence readings for no coagulation, $\Phi(r_{\mathrm{coag}} = 0)$. A key observation is that as the coagulation front ‘passes’ a sensor, there is an immediate rise in light intensity indicative of the location of the coagulation boundary. Figure 3(a) also shows for $r_{\mathrm{coag}} = 2$ mm, the light intensity at 2 mm and 8 mm

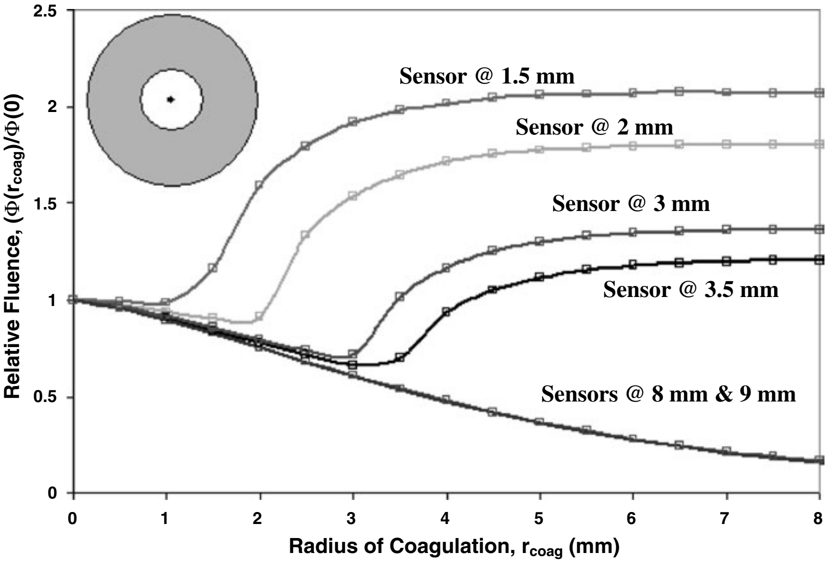

(a)

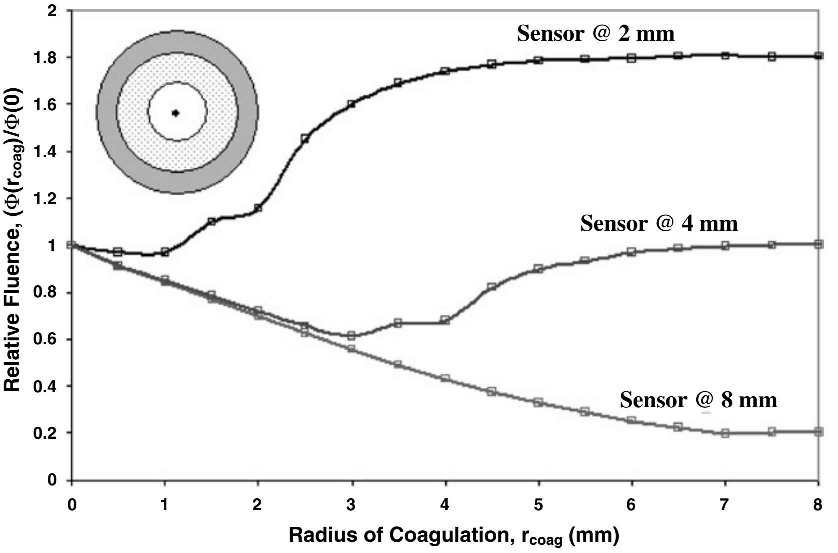

(b)

Figure 3. (a) Two-region (inset) MC results demonstrating changes in fluence, at several locations in the medium, due to increasing radii of coagulation. Note that for spatial locations inside the radius of coagulation, there is an increase in fluence; a decrease in fluence occurs for regions outside the radius of coagulation. (b) Three-region (inset) MC results demonstrating changes in fluence value due to increasing radii of coagulation of fully coagulated albumen phantom and with a 1 mm radius ring of partially coagulated properties at 2, 4 and 8 mm. Coagulation radii refer to the region with fully coagulated (region I) properties. In contrast to (a), instead of a decrease in fluence, a steady increase in fluence is observed as the coagulation front approaches and passes the 2 mm location. Locations outside the region of coagulation (8 mm) remain unchanged by the addition of the partially coagulated layer.

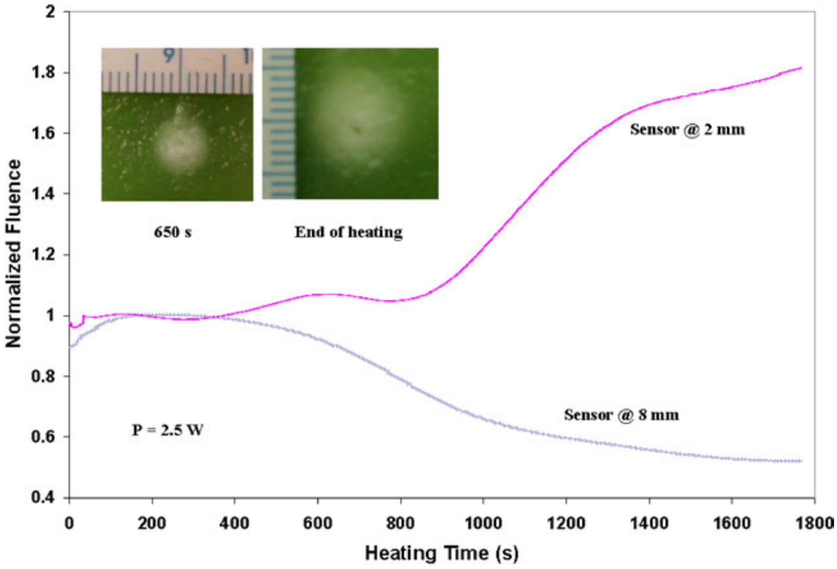

Figure 4. Changes in transient light intensity in albumen phantom measured interstitially during LITT at 2.5 W for ~1800 s. The final measured coagulation radius was 3.5 ± 0.5 mm. Insets are representative photographs of the coagulation region after 650 s and at the end of heating.

decreases to 0.9 and 0.75, respectively, while for $r_{\text{coag}} = 3.5$ mm, there is a subsequent increase at 2 mm to 1.65 and a decrease at 8 mm to 0.54. In addition, note that at 2 mm and 3.5 mm, errors in sensor placement may result in significant quantitative differences in fluence, particularly near the coagulation boundary. For example, given a coagulation radius of 3.5 mm, a 0.5 mm shift in sensor position from 2 → 1.5 mm or 3.5 → 3 mm will result in ~20% or ~45% differences in relative fluence, respectively. In contrast, a positioning error from 8 mm to 9 mm produces less than a 1% change in fluence.

While figure 2 represents the 'static' case of a fixed zone of coagulation following LITT, figure 3(a) represents the 'dynamic' change in light due to a growing coagulation front. In particular, figure 3(a) may be a more accurate representation of a coagulation formation during the *early* stages of a high power laser treatment, where the high-energy deposition and steeply attenuated fluence distribution generally results in a well-demarcated boundary of coagulation. By contrast, figure 3(b) shows the equivalent graph as figure 3(a), for a three-region MC. Figure 3(b) might represent the transient light intensity changes expected *early* during longer low power treatments where coagulation arises largely from thermal diffusion, thereby producing a gradually growing gradient of coagulation. Note that instead of a sharp drop prior to passing the 2 mm position as seen in the two-region model results, the relative fluence dips slightly, then increases to 1.10 and 1.17 as the coagulation size increases to 1.5 mm and 2 mm, respectively. After passing 2 mm, the light intensity then rises sharply, eventually plateauing at ~1.80. At a further distance of 8 mm, results of the three-region model exhibit little qualitative differences in light intensity changes compared to the two-region model and only minimal quantitative differences (10% difference for a coagulation radius of 3.5 mm).

4.2. Dynamic fluence changes in albumen phantoms—2.5 W, 1800 s

Figure 4 displays representative experimental results showing dynamic changes in light intensity measured in albumen phantoms during LITT at 2.5 W over ~1800 s of irradiation.

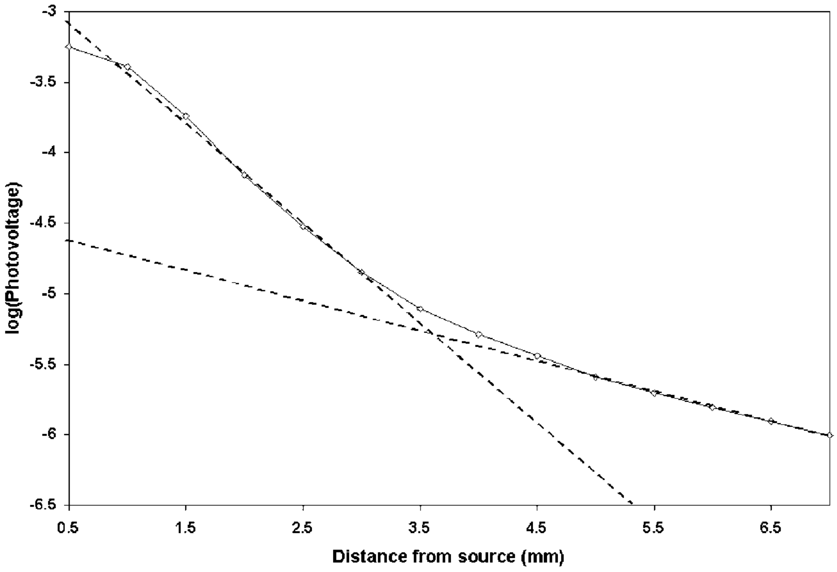

Figure 5. Measured spatial distribution of interstitial fluence in albumen phantom following LITT at 2.5 W for ∼1800 s. The intersection point of the two asymptotic slopes indicates a radius of coagulation of 3.5 ± 0.5 mm compared to the visually measured radius of 4 ± 0.5 mm. The dashed lines indicate asymptotic slopes and are included as guides to the eye.

Both the 2 mm and 8 mm detectors experience a slight initial rise in fluence that plateaus within the first 200 s of irradiation. This phenomenon was previously determined to be a 'photobleaching' effect caused by a decrease of the absorption properties of naphthol green dye at high power densities near the source fibre (Chin *et al* 2001). Visual examination of albumen phantoms following a similar but shorter irradiation scheme (2.5 W, 200 s) showed no evidence of coagulation. We thus normalized our fluence values to the point at $t = 200$ s, after the slight photobleaching rise had levelled off.

At ∼650 s, the fluence readings changed to 1.05 and 0.8 at 2 mm and 8 mm, respectively. This is in good quantitative agreement with the three-region MC model for a 1.5 mm coagulation radius, which predicts a change to 1.10 and 0.8 at 2 mm and 8 mm, respectively (figure 3(b)). Visual inspection of the lesion following ∼650 s (in different phantoms) showed a bright white 1.5 mm radius central zone surrounded by a lighter diffuse zone that extended to a radius of 2.5–2.75 mm (left inset, figure 4). Furthermore, at the end of the irradiation (∼1800 s), the measured fluence changes to 1.80 and 0.50 at 2 mm and 8 mm, respectively, which is in reasonable agreement with both three-region (1.69 at 2 mm, 0.49 at 8 mm) and with two-region (1.65 at 2 mm, 0.54 at 8 mm) MC results for a final coagulation radius of 3.5 mm. We posit that a spatial scan of the fluence distribution in the albumen phantom after heating should, therefore, show a point of intersection between the coagulated and native slopes at ∼3.5 mm (see figure 2). Figure 5 plots this fluence spatial distribution on a log scale. As expected, visual extrapolation of the intersection point from figure 5 indicates the coagulation zone to be 3.5 ± 0.5 mm in radius, which was in reasonable agreement with a visually measured final radius of 4.0 ± 0.5 mm. The visually measured coagulation radius was measured to the edges of the diffuse outer boundary (right inset, figure 4). Table 2 summarizes the results from the remaining three albumen phantom sets performed using the low power irradiation scheme. Results agree to within ∼30% with both two-region and three-region MC.

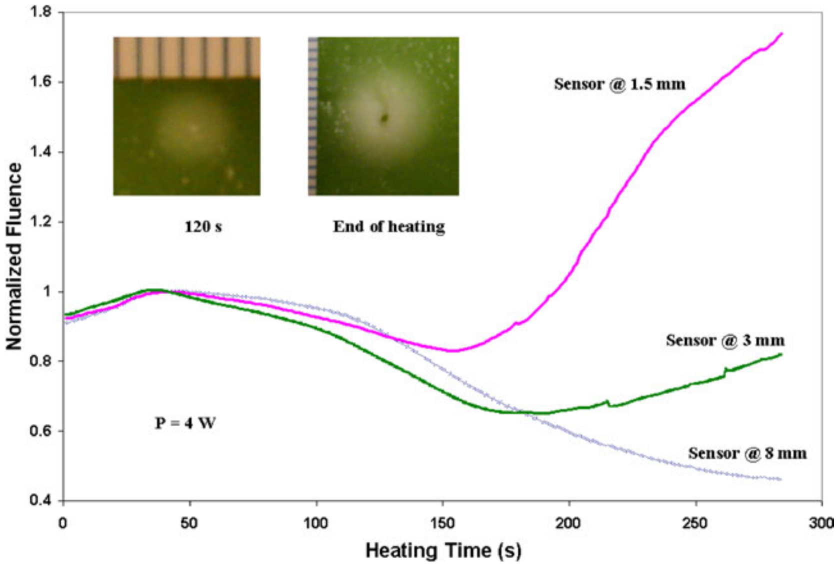

Figure 6. Changes in transient light intensity in albumen phantom measured interstitially during LITT at 4 W for ~275 s. The final coagulation radius was measured to be 4.0 ± 0.5 mm. Insets are representative photographs of the coagulated region after 120 s and at the end of heating.

Table 2. Final relative fluence values, $\Phi\,(t_{\mathrm{end}})/\Phi\,(0)$, for 3.5 ± 0.5 mm coagulation radius produced by 2.5 W irradiation for t_{end} seconds (~1800 s).

Sensor position (mm)	Two-region MC	Three-region MC	Experiment	Two-region deviation (%)	Three-region deviation (%)
2	1.65	1.69	2.04	24	21
			1.83	10	8
			1.80	9	7
			2.17	32	28
8	0.54	0.49	0.64	19	31
			0.59	9	20
			0.50	7	2
			0.50	7	2

4.3. Dynamic fluence changes in albumen phantoms—4 W, 275 s

Figure 6 shows the measured changes in fluence (normalized to $t \sim 35$ s to account for photobleaching) for sensors placed 1.5, 3 and 8 mm from the source during irradiation at 4 W. Unlike the 2.5 W case (figure 4), the early changes in light intensity exhibited better qualitative agreement with two-region MC results. A distinct drop in light intensity (to 0.83) is observed for the 1.5 mm sensor prior to the increase in light intensity due to the passing of the coagulation front, compared to a MC predicted decrease to 0.90 (at 2 mm). Two-region MC results at 3 mm and 8 mm for a 2 mm coagulation radius predict a decrease to ~0.75 for both locations, which agrees well with the experimentally measured values of ~0.75 at $t \sim 160$ s of heating. Typical coagulated regions following ~160 s heating in different phantoms exhibited a two-region appearance (left inset, figure 6). At the end of heating, a spatial scan similar to figure 5 was used to estimate the radius of coagulation at the intersection point, which indicated a coagulation radius of 4.0 ± 0.5 mm radius, compared with the visually

Table 3. Final relative fluence values, $\Phi(t_{\text{end}})/\Phi(0)$, for 4.0 ± 0.5 mm coagulation radius produced by 4 W irradiation for t_{end} seconds (∼300 s).

Sensor position (mm)	Two-region MC	Three-region MC	Experiment	Two-region deviation (%)	Three-region deviation (%)
1.5	2.01	2.00	2.25	12	13
			1.74	13	13
			2.03[a]	1	2
2	1.71	1.74	1.81[a]	6	4
3	1.16	1.22	0.56	51	54
			0.82	29	33
3.5	0.93	0.96	0.89[a]	4	7
4	0.55	0.68	0.58[a]	5	15
8	0.48	0.43	0.43	10	0
			0.46	4	9
			0.57[a]	19	32
			0.56[a]	17	30

[a] Datasets that were corrected for optical jumps.

measured coagulation radius of 4.5 ± 0.5 mm (right inset, figure 6). Visually, it is interesting to note that the *final* coagulation zone exhibits a three-region appearance, which suggests that during heating the thermal lesion evolved from two to three regions.

Final normalized fluence values were measured to be 1.74 (at 1.5 mm), 0.82 (3 mm) and 0.46 (8 mm), compared to three-region (2.00 at 1.5 mm, 1.22 at 3 mm 0.43 at 8 mm) and two-region (2.01 at 1.5 mm, 1.16 at 3 mm, 0.48 at 8 mm) MC predicted values. Table 3 summarizes the results for the four phantoms at high powers. Results agreed to within ∼30% for both two-region and three-region MC predictions, except for a single measurement at 3 mm which deviated by ∼50%. The 3 mm reading deviates significantly from theory; however, in section 4.1, the two-region MC results in figure 3(a) show that small errors in sensor positioning within 2–4 mm of the source can result in discrepancies of >100% in measured fluence. A retrospective analysis suggested that the sensor expected at 3 mm was likely to be located at ∼4 mm. Such positioning uncertainty is reasonable given the large expected fluence errors for small displacements close to the source. At 4 mm, experimental data exhibited quantitative agreement to within 2% with the MC predicted fluence.

We also note that during two of the experiments described in table 3 (denoted by the asterisks), sharp spikes in light intensity were observed that resulted in a sudden 15–20% increase in signal, particularly for sensors placed at 1.5 mm and 3.5 mm (not shown). Independent experiments in liver tissue indicate that the optical jumps might be a result of physical shifting of the optical sensor due to coagulation-induced shrinkage of the tissue. Such optical 'spikes' were ignored by subtracting this value from the measurements obtained for the remainder of the treatment (see section 5).

5. Discussion

During LITT, thermal coagulation results in a significant increase in the optical scattering properties of tissue. Therefore, using interstitial optical fluence sensors, light from the therapeutic fibre used to treat tumour tissue could simultaneously offer a means of probing the extent of thermal damage. Using appropriate opto-thermal denaturation models, such point optical information can then be extrapolated to reveal the full three-dimensional extent of thermal damage. However, the question arises as to the appropriate choice of light models for describing transient light intensity during different irradiation schemes.

We have examined the potential of both two-region and three-region spherical MC models to relate changes in measured fluence to coagulation size. To model a growing coagulation front, we have assumed that tissue coagulation will occur as a growing sphere of coagulated optical properties, centred at a 2 mm diameter source. As the coagulation front approaches a sensor, a drop in light intensity is predicted due to the higher scattering properties of the growing lesion trapping the light within the region of coagulation. This same light trapping effect results in an increase in light intensity following passage of the coagulation front. Such qualitative features were observed experimentally and predicted in our MC model. Ideally, figures 3(a) and (b) should represent the change in light intensity for any irradiation scheme, with the curves contracting at high rates of heating (figure 6) and expanding at lower heating rates (figure 4). However, especially close to the source (2–4 mm), distinct differences were observed between low and high power heating during early coagulation formation. At 4 W, an initial decrease in light intensity was observed while at 2.5 W, the fluence signal increased steadily during heating. These discrepancies might be attributed to differences in the progression of the coagulation front during fast and slow heating regimes.

At high powers, thermal coagulation forms quickly, with high-energy deposition rates limiting the influence of thermal conduction. During low power heating, the extent of thermal coagulation is governed primarily by the process of heat conduction. Due to the broader temperature gradient, coagulation evolves slowly; instead of an outwardly growing sharply demarcated radius, coagulation is distributed and diffuse with regions of partially coagulated tissue surrounding regions of fully coagulated tissue. We accounted for the differences in coagulation formation using a two-region MC to model well-demarcated coagulation formation, and a three-region MC to simulate the development of diffuse coagulation. For the three-region case, we approximated diffuse coagulation by adding an additional 1 mm ring with partially coagulated properties surrounding a fully coagulated sphere. The added layer enhances the light trapping effect and results in a greater build-up of diffuse light close to the source. This is in contrast to the two-region case, where no outer spherical shell is available to partially trap light, thereby allowing photons to escape from the coagulated region. Note that compared to the two-region model, when a sensor is not immediately in the vicinity of the boundary, adding the semi-coagulated layer will only result in a $\sim$10% change in relative light intensity.

Though not shown in the figures, another difference between high and low powered treatments was the appearance of optical spikes during 4.0 W heating, likely due to shrinkage of the albumen phantom during rapid heating of the phantom. In such cases, water is forced out quickly, producing tissue compression, desiccation and shrinkage, while maintaining the dry tissue mass (Pearce and Thomsen 1995). As the coagulation front passes an optical sensor, compression of the phantom material gradually pulls the optical sensor toward the source, culminating in a sudden shift in sensor position that manifests optically as a sudden increase or spike in light signal. This agrees with the observation that only during high power heating, sensors close to or within the region of coagulation (2–4 mm) exhibited significant optical spikes while sensors outside the coagulation zone (8 mm) demonstrated minimal artefact. We have previously observed shifts in sensor position during LITT of bovine liver.

It would also appear that the photobleaching effects observed early during irradiation does not confound our quantitative comparison with theoretical predictions. Photobleaching of the dye near the source may be due to a lowering of the absorption coefficient surrounding the fibres, thereby allowing greater penetration of light (Chin *et al* 2001). In our experiments, this leads to $\sim$10% increase in signal prior to coagulation. As previously stated in section 3, to account for this effect, we normalized our fluence data to the local maximum reading when the light intensity began to drop due to coagulation. Such normalization provides only a partial correction of the artefact, as photobleaching likely continues following the coagulation-induced decrease in fluence. As shown in tables 1 and 2, this might explain why the measured changes in light intensity were generally larger than those predicted by MC results. Though the full effects of photobleaching were not characterized, it appears that given the reasonable quantitative agreement with MC results, only minimal bleaching changes occur following coagulation. This may be because the change in μ_s' due to coagulation may be much greater than the change in μ_a due to photobleaching. Alternatively, to avoid photobleaching complications in phantoms, *ex vivo* liver tissue might be used for model studies, which exhibits minimal bleaching effects at room temperature (Chin *et al* 2001).

An important clinical implication of our MC model is that far from the source, changes in light intensity are weakly sensitive to sensor positioning errors. This is expected as the light field at a distance will be an averaged representation of the global coagulation state. This has both advantages and disadvantages: sensors placed near the source, in the direct zone of thermal damage, will be more sensitive to optical alterations but will also be highly sensitive to placement errors (for model agreement). To address the need for exact sensor placement, we have developed a strategy to locate the position of an array of fluence sensors relative to the source (Whelan *et al* 2001). In addition, a particularly promising result is that regardless of sensor positioning accuracy, passing of the coagulation front will result in an increase in measured fluence. Hence, in a clinical case, if optical sensors are placed at a desired treatment boundary, an increase in light intensity will signal to the clinician to terminate a treatment. We note that the finite size of commercially available light sensors (such as the 0.8–1.2 mm diameter fibres used in this study) might have the effect of slightly blurring the sharp increase that would be expected for an ideal point detector as the coagulation front passes. Clinically, consideration must be given to finding a balance between improving spatial sensitivity and the increasing fragility that is inherent in smaller detectors.

We also note that in simulations, the boundary of coagulation is readily determined by the sharp change in slope where the coagulated and native regions meet. However, this sharp boundary is ‘smeared’ out experimentally due to the diffuse nature of the edge of the resulting lesion. To account for this ‘smearing’ effect, we look for the intersection point between the maximum (coagulated) and minimum (native) slopes to give an effective two-region boundary that best represents the light intensity of a diffuse zone. Though this method provides only an approximation, it is interesting to note that despite appearing visually as three regions, light intensity changes due to the coagulated region exhibited slightly better quantitative agreement (generally within 20%) with two-region than three-region MC predictions.

Though representing the coagulated region as a sharply demarcated homogenous region may be an oversimplification, a two-region MC model does provide a direct mapping between a given change in light intensity and coagulation radius. Specifically, a two-region analytic diffusion theory model (Iizuka *et al* 2000) might be applied for online determination of coagulation size prior to and following the passage of the coagulation front during LITT treatments employing high powers. Further work is necessary to determine if such a multi-region diffusion theory model will allow for the accurate convergence of a solution when applied to the inverse problem of determining coagulation size. We are currently performing a MC based investigation to examine the applicability of the two- or three-region diffusion theory to assess coagulation size in typical biological tissues. As an example, figure 7 presents two-region MC light intensity profiles using prostate and liver optical properties, as shown in table 1. Note the sharper decrease in light intensity expected in liver compared to prostate as the coagulation front approaches each sensor and the smaller increase in light intensity following passing of each sensor. This difference is due to the 3× increase in liver absorption

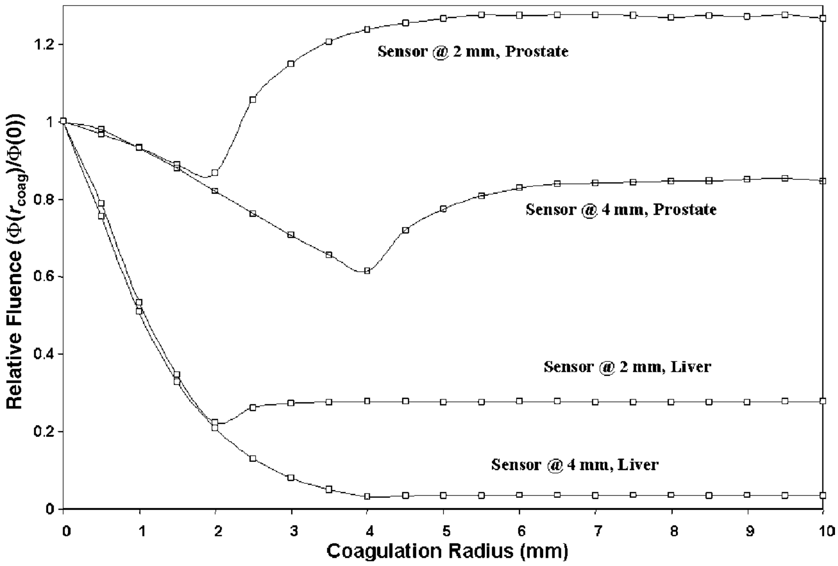

Figure 7. Two-region MC results demonstrating changes in light intensity, at two locations in the medium, due to increasing radii of coagulation for liver and prostate tissue. Note the sharper decrease in light intensity expected in liver compared to prostate as the coagulation front approaches each sensor and the smaller increase in light intensity following passing of each sensor. This difference is due to the 3× increase in liver absorption properties due to coagulation compared to prostate where absorption remains approximately constant.

properties due to coagulation compared to prostate where absorption remains approximately constant. Such results can then be used to test the validity of analytic multi-region models and test the fundamental limitations of optical monitoring for different background optical properties.

6. Conclusions

We have developed and utilized spherical two- and three-region MC models and experimental measurements in well-characterized albumen phantoms to better understand interstitial changes in light intensity that occur during LITT. During irradiation, dynamic changes in light intensity measured at various sensor positions showed good qualitative agreement with MC predicted changes in relative fluence due to increasing coagulation radii. A two-region model appears to better describe the transient light intensity changes early during high power treatments, while a three-region model might be more appropriate for low power cases and at the end of high power treatments. Post treatment, final light intensity changes and measured coagulation radius agree quantitatively with those predicted by two- and three-region MC simulation results for both heating schemes. The results suggest that interstitial light intensity measurements combined with multi-region light models may be used to infer the extent of thermal coagulation during LITT.

Acknowledgments

Financial support for this work was provided by the National Cancer Institute of Canada (with funds from the Canadian Cancer Society) and the Natural Sciences and Engineering Research

Council of Canada. The authors would like to thank Arthur Worthington, Ed Sinofsky, Vanessa Choy, Anoja Giles and Sean Davidson for experimental assistance. Also, special thanks to Michael Sherar and Lothar Lilge for helpful discussions and scientific advice.

Appendix. Ray tracing of a spherical object

Ray-tracing algorithms have long been employed for the purposes of graphics rendering. Though the concept of combining MC and ray tracing has been utilized in the past, such simulations have focussed on surface reflections of arbitrarily shaped objects (Glassner 1989) from external light sources. Here, we have developed the application of a combined MC ray-tracing simulation for internal light distributions. While the MC simulation models the behaviour of photons in turbid media, the ray-tracing algorithm is used to determine the location and instance when a photon crosses from one region of optical properties to another region of different optical properties. The basics of tracing a light ray passing through a spherical object are briefly outlined. A complete review of ray-tracing techniques is available (Glassner 1989).

The equation of a sphere centred on an arbitrary origin (x_c, y_c, z_c) is given by

$$(x - x_c)^2 + (y - y_c)^2 + (z - z_c)^2 = r^2. \tag{A.1}$$

During a MC simulation, the program samples random directional vectors μ_x, μ_y and μ_z. The line of sight vector originating from a point (x_0, y_0, z_0) has the following orthogonal components:

$$P_x = x_0 + \mu_x t \tag{A.2}$$

$$P_y = y_0 + \mu_y t \tag{A.3}$$

$$P_z = z_0 + \mu_z t. \tag{A.4}$$

Here t is a scaling constant equivalent to a ray's time of travel (also known as hit time) or mean free path. To calculate the intersection of a MC generated line of sight vector (P_x, P_y, P_z) with a point (x, y, z) on a sphere, we substitute (A.2), (A.3), (A.4) into (A.1) to give

$$\begin{aligned}\left(x_c^2 + y_c^2 + z_c^2\right) t^2 &+ 2(x_c(x_c - \mu_x) + y_c(y_c - \mu_y) + z_c(z_c - \mu_z)) + (x_0 - \mu_x)^2 \\ &+ (y_0 - \mu_y)^2 + (z_0 - \mu_z)^2 - r^2 = 0.\end{aligned} \tag{A.5}$$

Notice that (A.5) is arranged in the form $At^2 + 2Bt + C = 0$. Solving (A.5) using the quadratic formula we find

$$t = -B \pm \frac{\sqrt{B^2 - AC}}{A} \tag{A.6}$$

where $A = \mu_x^2 + \mu_y^2 + \mu_z^2$, $B = \mu_x(x_0 - x_c) + \mu_y(y_0 - y_c) + \mu_z(z_0 - z_c)$ and $C = (x_0 - x_c)^2 + (y_0 - y_c)^2 + (z_0 - z_c)^2 - r^2$.

The discriminant $\bar{D} = B^2 - AC$ will indicate one of three possibilities (see figure 1). If $\bar{D} < 0$, then the ray completely misses the sphere. If $\bar{D} = 0$, the ray grazes the sphere surface. Finally, if $\bar{D} > 0$, the ray is along the same line of sight as the sphere. Note that this does *not* indicate that the ray actually hits the sphere since we must also consider the photon's current path length. With $\bar{D} > 0$, solving for (A.6) gives two values for t. The resulting values for t offer important information regarding the direction of the photon. If both the values are positive, then the ray originated outside the sphere and the smaller value is the hit time as the ray enters the sphere while the larger value is the hit time as the ray leaves the sphere (after passing through). Since the ray will likely have changed directions in biological tissue before leaving the sphere, the hit time of interest in our simulations is always the smaller of the two values. If both values are negative, the ray is along the same line of sight as the sphere, but travelling away from the sphere. If one value is positive and the other negative, the photon is within the sphere and the positive value is the distance of intersection for the ray travelling in its current direction while the negative value represents the distance of intersection if the photon reversed its current direction. Finally, if one of the hit times is zero, the photon is currently on the sphere surface and we are interested in the other hit time only if it is positive. By determining t, we can apply equations (A.1)–(A.4) to determine the point of intersection at the sphere surface.

References

Alexandrakis G, Farrell T J and Patterson M S 1998 Accuracy of the diffusion approximation in determining the optical properties of two-layered turbid medium *Appl. Opt.* **37** 7401–9

Bennedbaek F N, Karstrup S and Hegedus L 2001 Ultrasound guided laser ablation of a parathyroid adenoma *Br. J. Radiol.* **74** 905–7

Bevan P and Sherar M D 2001 B-scan ultrasound imaging of thermal coagulation in bovine liver: frequency shift attenuation mapping *Ultrasound. Med. Biol.* **27** 809–17

Bremer C, Kreft G, Filler T and Reimer P 2002 Accuracy of non-enhanced MRI to monitor histological lesion size during laser-induced interstitial thermotherapy *Eur. Radiol.* **12** 5–6

Cheong W F, Prahl S A and Welch A J 1990 A review of the optical properties of biological tissues *IEEE J. Quantum Electron.* **26** 2166

Chin L C L, Whelan W M, Sherar M D and Vitkin I A 2001 Changes in relative light fluence measured during laser heating: implications for optical monitoring and modeling of interstitial laser photocoagulation *Phys. Med. Biol.* **46** 2407–20

De Jode M L 1999 Monte Carlo simulations of the use of isotropic light dosimetry probes to monitor energy fluence in biological tissues *Phys. Med. Biol.* **44** 3027–37

Eyrich G K, Bruder E, Hilfiker P, Dubno B, Quick H H, Patak M A, Gratz K W and Sailer H F 2000 Temperature mapping of magnetic resonance-guided laser interstitial thermal therapy (LITT) in lymphangiomas of the head and neck *Lasers Surg. Med.* **26** 467–76

Glassner A S (ed) 1989 *An Introduction to Ray Tracing* (New York: Academic)

Henyey L G and Greenstein J L 1941 Diffuse radiation in galaxy *Astrophys. J.* **93** 70–83

Iizuka M N, Sherar M D and Vitkin I A 1999 Optical phantom materials for near infrared laser photocoagulation studies *Lasers Surg. Med.* **25** 159–69

Iizuka M N, Vitkin I A, Kolios M C and Sherar M D 2000 The effects of dynamic optical properties during interstitial laser photocoagulation *Phys. Med. Biol.* **45** 1335–57

Kienle A, Patterson M S, Dognitz N, Bays R, Wagnieres G and van den Bergh H 1998 Noninvasive determination of the optical properties of two-layered turbid media *Appl. Opt.* **37** 779–91

Martelli F, Bassani M, Alianelli L, Zangheri L and Zaccanti G 2000 Accuracy of the diffusion equation to describe photon migration through an infinite medium: numerical and experimental investigation *Phys. Med. Biol.* **45** 1359–73

Patterson M S, Wilson B C and Wyman D R 1991 The propagation of optical radiation in tissue II *Lasers Med. Sci.* **6** 155–68

Pearce J and Thomsen S 1995 Rate process analysis of thermal damage *Optical-Thermal Responses of Laser-Irradiated Tissue* ed A J Welch and M J C van Gemert (New York: Plenum)

Pham T H, Spott T, Svaasand L O and Tromberg B J 2000 Quantifying the properties of two-layered turbid media with frequency-domain diffuse reflectance *Appl. Opt.* **39** 4733–45

Purdie T G, Lee T-Y, Iizuka M and Sherar M D 2000 Dynamic contrast enhanced CT measurement of blood flow during interstitial laser photocoagulation: comparison with an Arrhenius damage model *Phys. Med. Biol.* **45** 115–1126

Ritz J P, Roggan A, Isbert C, Muller G, Buhr H G and Germer C T 2001 Optical properties of native and coagulated porcine liver tissue between 400 and 2400 nm *Lasers Surg. Med.* **29** 205–12

Roggan A and Muller G (ed) 1995 Dosimetry and computer-based irradiation planning for laser-induced interstitial thermometry (LITT) *Laser-Induced Interstitial Thermotherapy* (Bellingham, WA: SPIE Optical Engineering Press)

Sherar M D, Gertner M R, Yue C K, O'Malley M E, Toi A, Gladman A S, Davidson S R H and Trachtenberg J 2001 Interstitial microwave thermal therapy for prostate cancer: method of treatment and results of a phase I/II trial *J. Urol.* **166** 1707–14

Sherar M D, Moriarty J A, Kolios M C, Chen J C, Peters R D, Ang L C, Hinks R S, Henkelman Rm, Bronskill M J and Kucharcyk W 2000 Comparison of thermal damage calculated using magnetic resonance thermometry, with magnetic resonance imaging post-treatment and histology, after interstitial microwave thermal therapy of rabbit brain *Phys. Med. Biol.* **45** 3563–76

Skinner M G, Everts S, Reid A D, Vitkin I A, Lilge L and Sherar M D 2000 Changes in optical properties of *ex vivo* rat prostate due to heating *Phys. Med. Biol.* **45** 1375–86

Svaasand L O, Spot T, Fishkin J B, Pham T, Tromberg B J and Berns M W 1999 Reflectance measurements of layered media with diffuse photon-density waves: a potential tool for evaluating deep burns and subcutaneous lesions *Phys. Med. Biol.* **44** 801–13

Van Staveren H J, Marijinisson J P A, Aalders M C G and Star W M 1995 Construction, quality assurance and calibration of spherical isotropic fiber optic light diffusers *Lasers Med. Sci.* **10** 137–47

Vitkin I A *et al* 1997 Magnetic resonance imaging of temperature changes during interstitial microwave heating: a phantom study *Med. Phys.* **24** 269–77

Wang L, Jacques S L and Zheng L 1995 MCML-Monte Carlo modelling of light transport in multi-layered tissues *Comput. Methods Programs Biomed.* **47** 131–46

Whelan W M 1996 Dynamic modeling of ILP in soft tissue *MSc Thesis* McMaster University, Hamilton, Ontario

Whelan W M, Chun P, Chin L C L, Sherar M D and Vitkin I A 2001 Laser thermal therapy: utility of interstitial fluence monitoring for locating optical sensors *Phys. Med. Biol.* **46** N91–6

Wilson B C and Adam G 1983 A Monte Carlo model for the absorption and flux distributions of light in tissue *Med. Phys.* **10** 824–30

Wohlgemuth W A, Wamser G, Reiss T, Wagner T and Bohndorf K 2001 *In vivo* laser-induced interstitial thermotherapy of pig liver with a temperature-controlled diode laser and MRI correlation *Lasers Surg. Med.* **29** 374–8